Microfluidic platform to transduce cell viability to distinct flow pathways for high accuracy sensing

Authors:

Fatima Ezahra Chrit¹, Abhishek Raj^{1,a)}, Katherine M. Young², Nicholas Stone¹, Peter Shankles¹, Kesiharjun Lokireddy¹, Christopher Flowers³, Edmund K. Waller³, Alexander Alexeev¹, Todd Sulchek^{1,*)}.

1.George W. Woodruff School of Mechanical Engineering, Georgia Institute of Technology, Atlanta, Georgia 30332, USA

- 2. The Wallace H. Coulter Department of Biomedical Engineering, Georgia Institute of Technology & Emory University, Atlanta, Georgia 30332, USA
- 3. Winship Cancer Institute, Emory School of Medicine, 1365 Clifton NE Rd.: Atlanta, Georgia 30322, USA
- a) Present Address: Department of Mechanical Engineering, Indian Institute of Technology Patna, Bihar-801103, India

Abstract

Cells mechanical properties such as stiffness can act as biomarkers to sort or detect cell functional properties, such as viability. In this study, we report the use of a microfluidic device as a high sensitivity sensor that transduces cell biomechanics to cell separation to accurately detect viability. Cell populations are flowed and deflected at a number of skew ridges such that deflection per ridge, cell-ridge interaction time, and cell size, can all be used as sensor inputs to accurately determine cell state. The angle of the ridges was evaluated to optimize the differences in cell translation between viable and non-viable cells while allowing continuous flow. In the first mode of operation, we flowed viable and non-viable cells through the device and conducted a sensitivity analysis by recording the cell's total deflection as a binary classifier that differentiates viable from non-viable cells. The performance of the sensor was assessed using an area under the curve (AUC) analysis to be 0.97. By including additional sensor inputs in the second mode of operation, we conducted a principal component analysis (PCA) to further improve the identification of cell state by clustering populations with little overlap between viable and non-viable cells. We therefore found microfluidic separation devices can be used to efficiently sort cells and accurately sense viability in a label-free manner.

Keywords: cell viability sorting, optical sensing, microfluidics, cell mechanics, label-free separation

^{*)} Author to whom correspondence should be addressed: todd.sulchek@me.gatech.edu

The knowledge of the cell viability is critical to understand and predict cell culture health (1, 2) and therapeutic responses to pharmacological agents (3). Yet, there exist few options for monitoring the viability and functional health of cells and cell products. Typically, technicians must periodically sample the culture to evaluate the cells manually using viability stains. This procedure is costly, risks contamination, and is not amenable to automation of decision making, i.e. whether to change culture conditions or when to harvest the culture. Furthermore, commonly used cell viability stains and conventional apoptosis assays can significantly underestimate the viability of cells (4, 5) and can lead to up to 40% false positive counts in both primary cells and cell lines (6), preventing accurate assessment of cell viability. The ability to detect changes in cell viability with single-cell resolution is also desired to detect early changes in culture health. Thus, there is a need for improved, label-free sensors to enable read out of cell viability.

In addition to sensing, removing non-viable cells can purify a culture and reduce unwanted byproducts from apoptotic cells. For example, in the final stage of cell therapy manufacturing, products must meet release criteria for viability, yet occasionally do not, which may prohibit the sale and add a substantial cost to the cell therapy manufacturer (7, 8). New methods to maintain specifications of a product through a simple purifying step of removing nonviable cells, with minimal loss of cell product, could therefore enhance the production reliability of cell therapies. In addition, removal of non-viable cells may improve the capacity of a culture to proliferate by reduction of negative signaling from cytokine release (9). Therefore, alternatives for removal of nonviable cells with minimal loss of cell product may substantially benefit cell culture and cell therapy.

To address the need to monitor and purify cells for viability, we highlight the use of physical changes that occur to cells after a loss of viability that could be leveraged in a label-free manner to sense and sort viable cells to substantially benefit cell manufacturing. The biophysical science community has documented a number of changes to cell biomechanics (10-14), electrical properties (15-17), and ion permeability (18-20) that can all correlate with loss of viability. In this context, microfluidic platforms have been used to separate viable from non-viable cells based on these differences. For example, di-electrophoresis (15, 21) and acoustophoresis (22) were both reported to sort viable cells. These approaches use physical changes to the cell upon apoptosis and show a range of sensitivity, i.e. ability to detect changes to individual cells, dynamic range, i.e. able to measure large number of cells, and time response, and ability to detect early changes to apoptotic cells (15, 23). Microfluidic approaches have many advantages to sense the properties of single cells through changes in biophysical properties (12, 24-27). Microfluidic platforms have moreover been used as sensors to measure changes in cell electrical properties (28) or deformability (29, 30).

In this study, we demonstrate a microfluidic technology that uses changes to cell biomechanics, including stiffness, to sense and enumerate cell viability in a manner that is label-free, accurate, continuously operating, and sensitive to individual cells at early time-points of apoptosis. Cell viability transduction performed by our microfluidic platform refers to the conversion of viability states into distinct flow patterns (step 1, accomplished by device) and secondly to a readout platform (step 2, implemented with video microscopy and data analytics). The microfluidic channel features skew diagonal ridges which deform flowing cells and transduce resistance to deformation as a deflection to trajectory. The

microfluidic technology also has the capacity to enrich viable from non-viable cells by collection to separate outlets, which has initially been shown in prior studies (26). In this work, we modify the microfluidic separation for "high sensitivity" operation by investigating the device and process parameters that magnify differences between viable and non-viable cell trajectories. We also explore new sensing modalities in which we detect changes in cell trajectories using optical video microscopy and cell tracking algorithm to identify distinct biomechanical properties that correlate with a loss of cell viability. With this core technology, we introduce the use of our microfluidic platform as a flow-based viability sensor that operates by separating different cell populations.

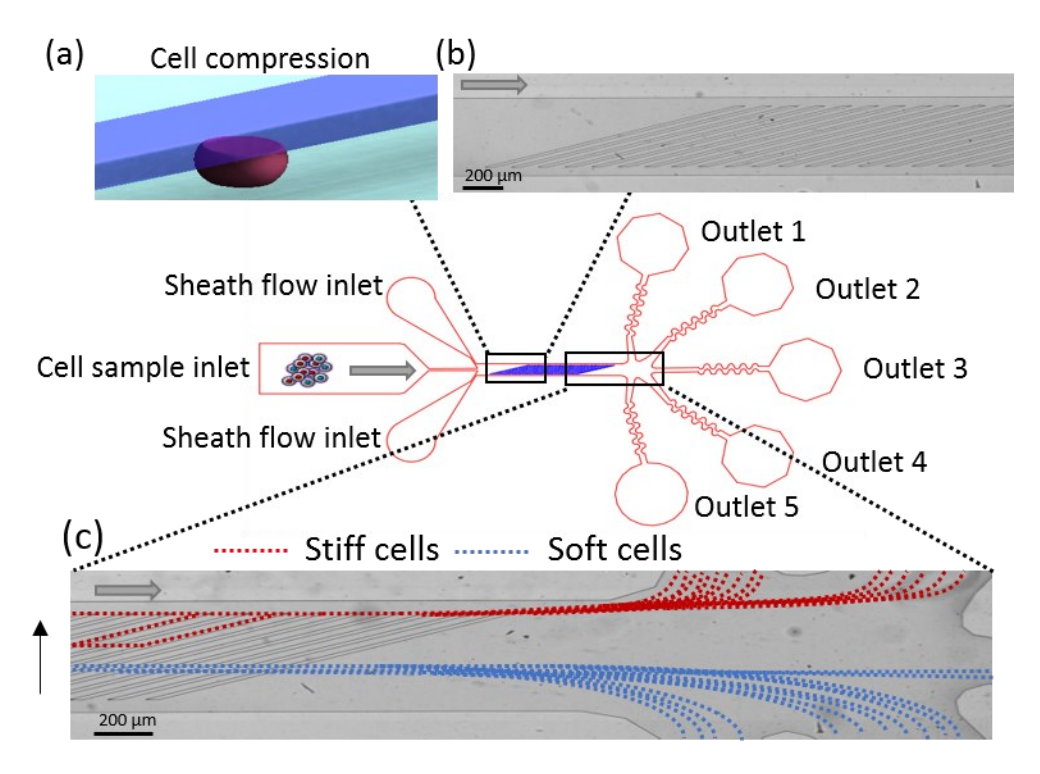


Figure 1: Cell sorting microfluidic device using diagonal ridges. (a) Schematic representation of cells compression under the ridge. (b) Optical micrograph of the fabricated device showing the first ridges. (c) Representative micrograph showing stiff and soft cells flowing towards different outlets. Horizontal arrows indicate the flow direction, the vertical arrow indicates the direction of positive deflection and dotted lines represent trajectory pathways within the device for stiff (red) and soft (blue) cells.

The microfluidic channel with diagonal ridges is shown in Fig. 1. Cells, containing both viable and non-viable populations, are infused from the cell sample inlet and are focused by two sheath flows before reaching the channel region with diagonal ridges. Cells are deformed under the ridges due to the gap size being smaller than the cell diameter (Fig. 1a) and translate in the direction transverse to the fluid flow in a manner dependent on the cellular mechanical properties. The precise trajectory is primarily due to the balance of two competing forces: the elastic force resulting from a resistance to deformation when in contact with the ridge and the hydrodynamic drag force that lead to a net force with a transversal component directly correlated with the cell stiffness. In the last region, five outlets are designed to sort cell populations into distributed and fractionated subsets with different cell stiffness. The stiffest cells flow towards the "stiff" outlet 1 and the softest cells are directed towards the "soft" outlet 5, while cells of moderate stiffness will flow in a graduated manner

to the central outlets 2, 3, and 4 respectively (Fig. 1c). The serpentine patterns before each outlet are added to limit channel flow biasing by increasing the flow resistance between the inlet and the outlet of the channel.

Materials and Methods

Device fabrication

The microfluidic device was fabricated using replica molding of polydimethylsiloxane (PDMS) on a SU-8 patterned silicon wafer (26, 31). The molds for the device were fabricated using a two-layer photolithography process in which SU-8 photoresist (SU-8 Microchem Corp.) was spin coated on a silicon wafer. The devices tested were designed using AutoCAD and the mold ridge gap size and other dimensions were measured after fabrication using optical microscopy and profilometry (Dektak 150 profilometer). The patterns were transferred from the mold using PDMS, mixed (10: 1 wt/wt) with Sylgard 184 silicone elastomer curing agent (Dow Corning). The mixture was then degassed in a vacuum chamber, poured on the mold and cured at 80 °C for 1 hour. The PDMS device was then peeled off the wafer, the inlet and outlet holes were punched using a biopsy punch, and the chip bonded to a glass slide after an air plasma treatment (PDC-32G Harrick). In order to prevent non-specific cell adhesion to the microfluidic channel, the device was passivated by coating with Bovine Serum Albumin (BSA, Sigma Aldrich) at a concentration of 10 mg/ml and incubated overnight at 4 °C. Alternatively, in some devices, we chose passivation by chemical vapor deposition of Triethoxysilane (3-Aminopropyl), purchased from Sigma-Aldrich. In a fume hood, a petri dish was placed on a hot plate with the cap of an Eppendorf tube. Bonded PDMS devices were plasma cleaned for 1 min and placed in the dish. 40 µl of Triethoxysilane was then added to the Eppendorf cap and the petri dish was covered. The petri dish was heated in an oven at 80 °C for 2 hours to complete the surface treatment. Silane passivation was specifically used in the experiments of Fig. 5a,b and some experiments used for PCA analysis in Fig. 9.

Cell preparation

Jurkat cells (CRL-1990) were purchased from ATCC. The cells were cultured and maintained in RPMI-1640 medium (Sigma) supplemented with 10% FBS and incubated at 37 °C with 5% CO_2 . To prepare the non-viable cell samples, the cells were heated at 60 °C in a water bath for 1 hour. The viability of cell samples was measured using 7-AAD staining (Biolegend) a membrane impermeable dye generally excluded from viable intact cells. In damaged cells, however, the dye is able to permeate compromised membranes and shows strong fluorescence at 647 nm. Cells are resuspended in 0.5 mL of cell staining buffer where 5 μ L of 7-AAD is added per million cells and incubated for 5-10 minutes in the dark before analysis. Flow cytometry was conducted to measure the frequencies of stained non-viable cells and non-stained viable cells. Heat treated cells showed more than 98% non-viable using 7-AAD assay, which confirms the heat induced cell death.

Experimental setup

Heat-treated and untreated cells were suspended in a Phosphate Buffer Solution (PBS) at $1-1.5 \times 10^6$ cells/ml and infused into the device inlet at specified flow rates using a syringe pump. The microfluidic chip was mounted on an inverted bright-field microscope (Eclipse Ti, Nikon) and cell trajectories were observed and recorded using a high-speed camera (Phantom V7.3, Vision Research) at a frame rate of 3000 frames per second.

Cell tracking algorithm

To enable high-throughput analysis of device sorting performance, a custom Python package was written to track cells in videos resulting from high-speed microscopy and convert collected tracks into a form suitable for quantitative comparison between experiments and videos. In order to accomplish this task, moving particles were first extracted from the stationary image background using standard background subtraction and thresholding methods and then joined into single cells 'paths' using a custom algorithm. This algorithm functions by considering detected moving objects as points in a three-dimensional space defined by the two in-plane dimensions and time as the third dimension. Points were linked into paths by linking points that are mutual nearest neighbors in this space and then cutting the longest links, which are most likely made up of points resulting from different cells. At this stage, these paths can give an overall impression of the trajectory of the cells but are not suitable for direct comparison between videos as the points on each path will be defined by their locations in an image rather than real-world dimensions relative to the device geometry. In order to address this point, the layout of the ridges was extracted from the video and compared to the known device geometry, allowing extracted paths to be related to their real location within the device. This step allowed paths and extracted metrics to be compared directly between experiments to directly compare experimental conditions and speed the process of sorting optimization.

Analysis of cell tracking result using Principal Component Analysis

Using custom Python software, we extracted cell trajectory data points from both viable and heat-treated non-viable cells moving through our microfluidic device, including amount of deflection at each ridge, duration of interaction at each ridge and the size of the cell while it is under the ridge and between ridges. The size of each tracked cell was recorded as a mean both under ridge and in between the ridges. If only one of the two size measurements was available, one value of cell size was recorded. Cells reach a maximum trajectory deflection when the gutter region is reached at the top channel wall shown in Fig. 1b. For cells directed to the gutter, trajectory values after reaching the gutter were imputed by taking the average of deflection at each ridge. Additionally, because the cells deflected to the gutter could no longer interact with the subsequent ridges, the interaction time for those cells directed to the gutter region were assigned as a value of -100 s to distinguish from other recorded values. We performed a principal component analysis (PCA) using R using complete datasets that were centered and scaled. The biplot was created using the package ggbiplot, grouping cells by their status as viable and non-viable from each condition.

AFM methodology

Atomic Force Microscopy (AFM, MFP-3D, Asylum Research) with an integrated optical microscope (Nikon) on a vibration isolation table was used to measure cell mechanical properties. For better global stiffness measurements of the cell, a 7.3 µm polystyrene sphere was attached to tipless silica nitride cantilevers (Bruker Probes) using a two-part epoxy and cured for at least 24 hours. For each cell, force-indentation curves were obtained using force spectroscopy. Before measurements, the AFM was calibrated by taking a single force curve on a clean FluoroDish (World Precision Instruments) to determine the deflection inverse optical lever sensitivity, which relates the voltage read in the photodetector to the amount of cantilever deflection for the particular cantilever. Next, the Sader calibration (32) method was used to obtain cantilever spring constants based on the thermal vibration of the cantilever, with an approximate value of 30 pN/nm. Cells were attached to a Fluorodish

using 3.5 ug/cm 2 CellTak Cell and Tissue Adhesive (Corning). For measurements, the cantilever probe was visually aligned with the cell center and moved with a velocity of 2 μ m/s to indent the cell with increasing compressive force until a force trigger of 5 nN was reached. The cantilever was held in position for 10 seconds, dwelling towards the surface, allowing for viscous relaxation of the cell before reversing the direction of its velocity.

We used custom code written in R implementing a Hertzian contact model to calculate the cellular Young's modulus (33) from the force curves. The Hertz model describes non-adhesive elastic contact between two bodies under a load. The contact point was estimated by the intersection of the flat, undeformed region of the force curve with a line fit to the force curve region where the cantilever was in contact with the cell. Next, we identified the true contact point by iteratively testing the points in proximity to the estimated contact point with the minimal residual difference between the measured force curve and a nonlinear fit described by the governing Hertz equation used to describe the contact between an elastic sphere and an elastic half space. Next, we used custom R code to fit the dwell region of the force curve to a biexponential decay curve to identify the fast and slow viscous time constants (34). We additionally used custom R code to determine the adhesion force between the probe and the cell of interest by subtracting the minimum measured force after retraction from the force measured at the cantilever's undeformed state. For every cell mechanically probed, we additionally captured an optical microscopy image to analyze size using ImageJ software by outlining each cell with an ellipse to record an area.

Results and Discussion

Characterization of viable and non-viable cells

AFM analysis of both viable and non-viable cells populations was conducted to quantify the biomechanical properties. The average Young's modulus was found to be 0.2 kPa for viable cells and 1.92 kPa for non-viable cells (p < 10^{-11} where p is the probability value of the null hypothesis for a conducted student t-test), indicating a significant increase of nearly one order of magnitude as shown in Fig. 2a. The dramatic increase in cell stiffness with cell death is a result of several structural changes to the cell, including to dynamic changes of actin fibers, the presence of stress fibers, cell wall modification, and changes of cortical actin organization under the cell membrane (12, 24, 25, 27).

We conducted an analysis of the viscoelastic properties of viable and non-viable cells by calculating viscoelastic time constants using Maxwell-Wiechert model (35) as shown in Fig. 2b. To best fit the data, two Maxwell elements were chosen: the slow and the fast relaxation time constant. The slow viscous time constant was found to be $0.41~\text{s}^{-1}$ for viable cells and $0.31~\text{s}^{-1}$ for non-viable cells (p < 10^{-11}), and the fast time constant was $5.75~\text{s}^{-1}$ for viable cells and $6.10~\text{s}^{-1}$ for non-viable cells (p < 0.24, data not shown). This result shows that the slow viscosity time constant of viable and non-viable Jurkat cells is also significantly different and thus, it can be considered as a viability marker.

We also measured the adhesion force of both viable and non-viable cells populations by examining the attraction between the cell and the AFM probe upon cell contact. The magnitude of the adhesion force was found to be 0.22 nN for viable cells and 1.05 nN for non-viable cells (p < 0.0001), as presented in Fig. 2c. This result shows that non-viable cells are more adhesive to the silica bead of the AFM tip than viable cells. Furthermore, the

same observation is noticeable during the experiments in which non-viable cells interact with the PDMS and glass surfaces of the microfluidic channel. The increased attractive interaction of the non-viable cells in comparison to viable cells could lead to adhesion to the ridges, an inhibition of continuous flow or a modification to the trajectory of flow (36).

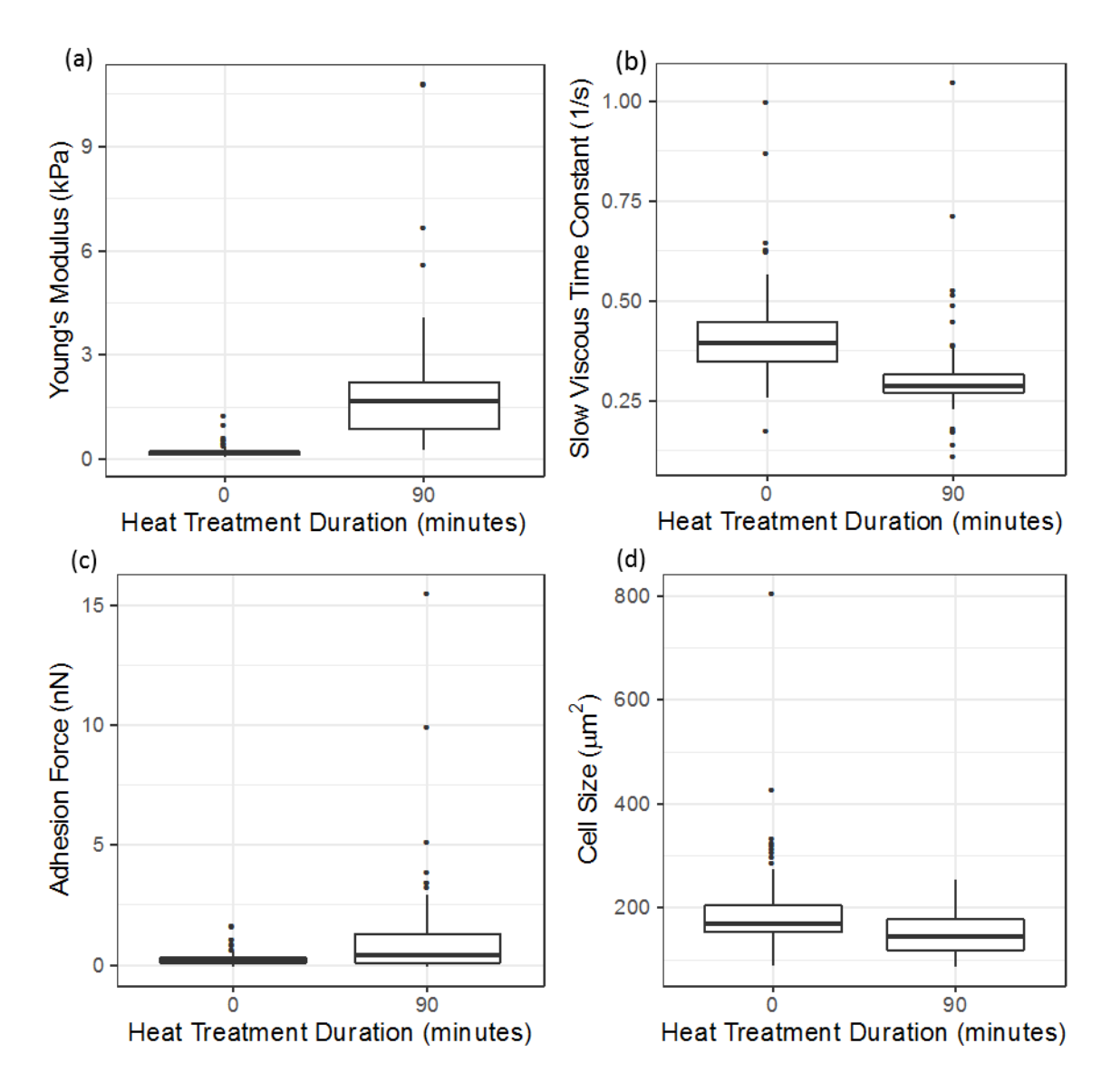


Figure 2: Mechanical properties of viable and non-viable Jurkat cells from AFM measurement. (a) Young's modulus (p-value < e-11). (b) Slow viscous time constant (p-value < e-11). (c) Adhesion force (p-value < 0.0001). (d) Cell apparent surface (p-value < e-7). Number of cells n=268.

The cell size was the final biomechanical property that we evaluated from analysis of optical images taken during AFM measurements. The average diameter was found to be 15.5 μ m for viable cells and 13.83 μ m for non-viable cells (p < 10⁻⁷). As shown in Fig. 2d, non-viable cells were found to be slightly smaller than viable cells at the time points recorded, which is in agreement with what was reported as a change in cell size during apoptosis and necrosis (24, 37), though we note that cell size can vary over the course of apoptosis. Overall, both stiffness and adhesion properties provide opportunities for viability markers due to the large differences between viable and non-viable cells. Thus, the

enrichment and separation between the two cells populations in microfluidic separation device likely rely on difference in these properties.

Microfluidic device design optimization

There are several device and process parameters that affect cell trajectories in the microfluidic channel, including the ridge gap, the ridge angle and the flow rate. The ridge gap, which is the distance between the ridge and the bottom channel surface, should depend on the target cell size. The gap size should be small enough to sufficiently compress cells, which have an average diameter of 15 μ m. On the other hand, the gap should be large enough to prevent channel occlusion. In this work, the ridge gap was chosen to be 8 μ m based on previous studies that suggest an optimal strain of 45% (31, 38) for cell sorting.

The ridge angle relative to the channel axis was tested as a parameter that can significantly increase the sensitivity of the cell separation by the microfluidic device. In previous studies (31, 38), we tested 45° and 30° ridge angles and found that they both lead to a small gradual displacement of stiff cells at each ridge, which adds up through the multiple ridges and results in the separation. However, at a smaller angle, i.e. more aligned with the channel axis, we observed a different type of stiff cell trajectories, in which cells primarily slide along the leading edge of a ridge to significantly enhance the separation (see Video S1, Video S2, and Video S3).

To better understand the effect of ridge angle and flow rate, we performed numerical simulations using our inhouse fluid-structure interaction model. To model particle compliance, we used the capillary number $Ca = \mu U/ED$, which describes the relative importance of viscous forces with respect to elastic compliance, where μ is the viscosity, U is the average fluid velocity, E is the cell Young's modulus and D is the cell diameter.

Fig. 3 shows a channel top view where fluid streamlines are plotted in red and cell trajectories in blue for (a) 40° and (b) 20° ridge angle devices. We observe that the stiff particle (solid blue line) deflects along the ridge in both devices whereas the softer particle (dashed blue line) only deflects in the 20° ridge angle device. In fact, for smaller ridge angles, the transverse component of the elastic force increases, leading to more displacement along the ridge. Thus, ridge angle can be tuned to deflect non-viable cells with a wider range of capillary numbers, which leads to a greater sorting sensitivity.

We also probe the effect of flow rate by modeling the motion of cells using three different flow rates in a 40° ridge angle device. As shown in Fig. 3c, increasing the flow rate drives the cell to squeeze under the ridge due to an increase in the hydrodynamic drag force. We therefore conclude that the flow rate is a critical parameter that should be controlled to enhance the separation.

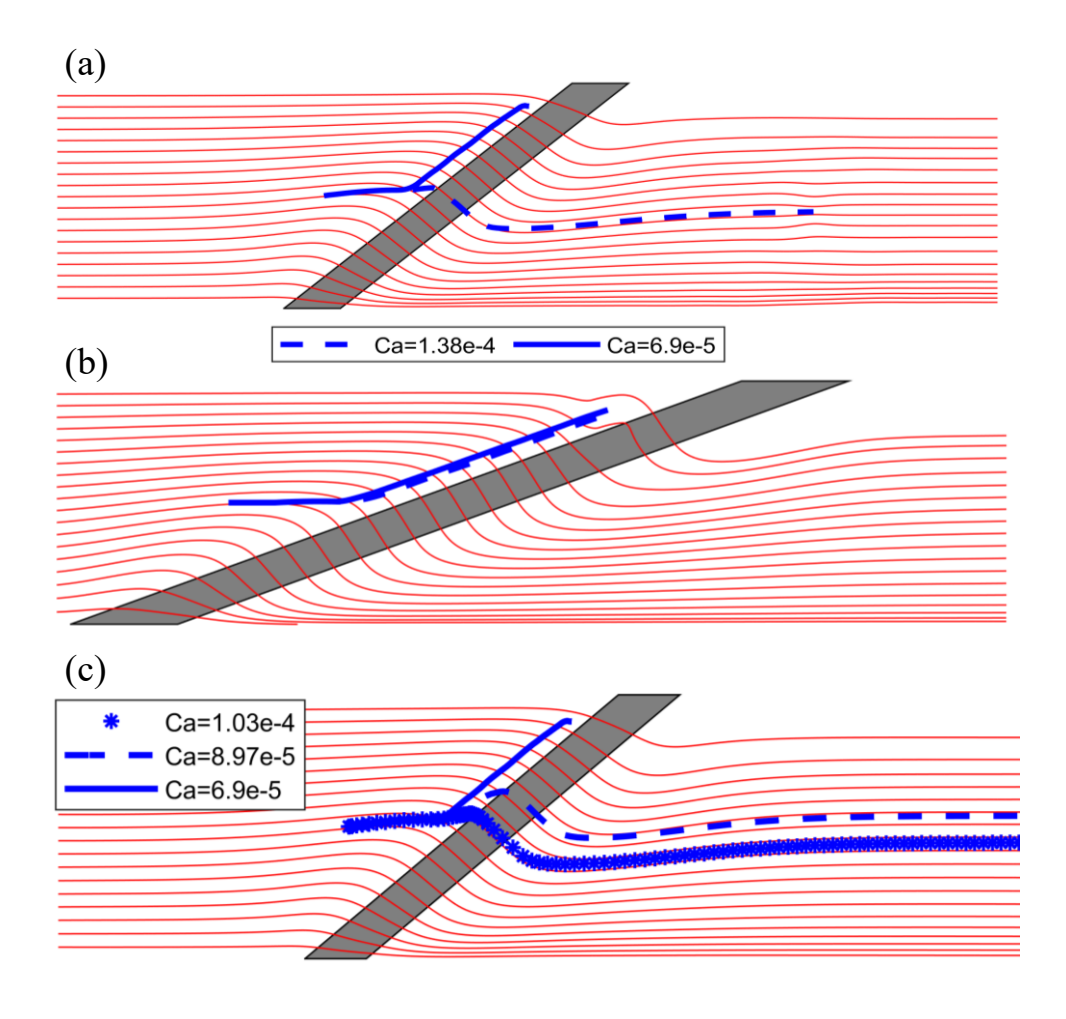


Figure 3: Channel top view. Fluid streamlines (red) and cell trajectories (blue) in (a) 40° and , (b) 20° ridge angle devices at the same flow rate and (c) 40° ridge angle at three different flow rates.

Experimentally, we investigated smaller ridge angles of 20°, 15°, and 10° to separate viable and non-viable cells. For non-viable cells, the three angles act similarly with 80% of the cells dispersed towards the stiff outlet 1, as shown in Fig. 4a. For viable cells, more than 70% of the cells are directed to the soft outlets 4 and 5 when using 20° and 15° ridge angles, whereas for 10° angle, less than 45% of the cells end up in the soft outlets and around 25% of cells were directed towards the stiff outlet 1, overlapping with non-viable cells, as shown in Fig. 4b. We conclude then that 10° ridge angle results in an excessive cell displacement due to the elastic force leading to the translation of the soft cell population along the ridges, which lowers the separation resolution. The best separation occurred using the 20° and 15° ridge angle.

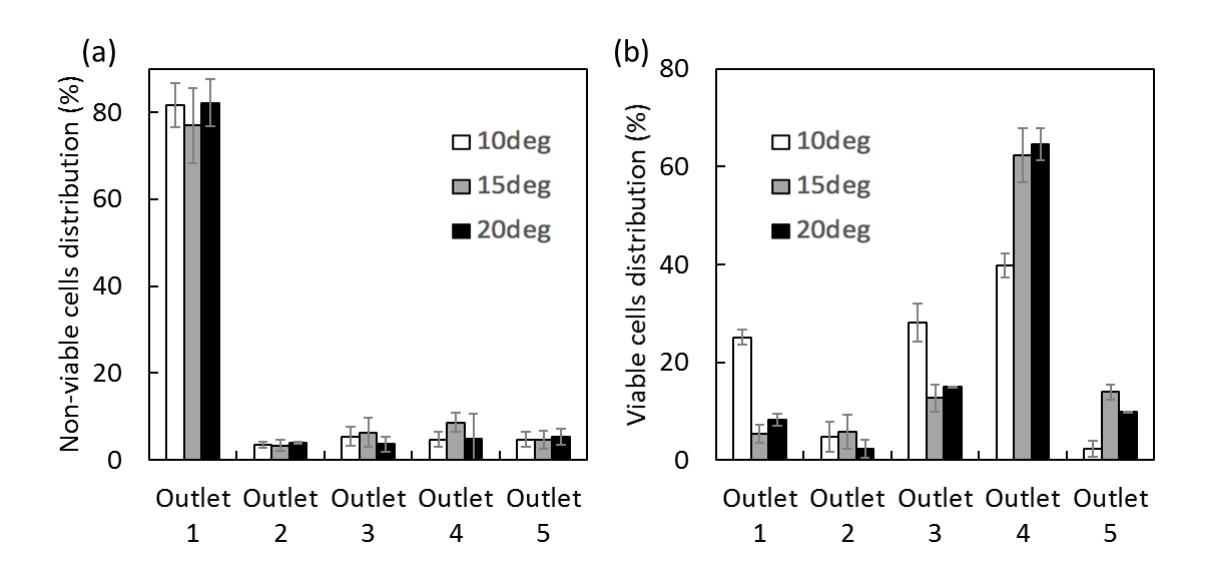


Figure 4: (a) Non-viable and (b) viable Jurkat cells distribution at the five different outlets after sorting. Cells were flown at 35μ l/min in three different ridge angle devices: 20° , 15° and 10° .

Next, we analyzed the effect of the flow rate on the trajectories of different cell types in a device with the ridge angle equal to 20° . Non-viable and viable Jurkat and SUDHL cells were flowed separately at different flow rates: $35\mu l/min$, $65\mu l/min$ and $115\mu l/min$. The distributions of these cells at the outlets are shown in Fig. 5. We find that at a lower flow rate of $35\,\mu l/min$, more than 80% of non-viable cells were translated towards the stiff outlet 1, whereas at a higher flow rate of $65\mu l/min$, only around 47% of non-viable cells migrate towards outlet 1 and the rest of these cells are directed to the softer outlets, overlapping with viable cells. At the highest flow rate of $115\,\mu l/min$, only 20% of non-viable cells translate towards the stiff outlet 1 leading to a poor cell separation.

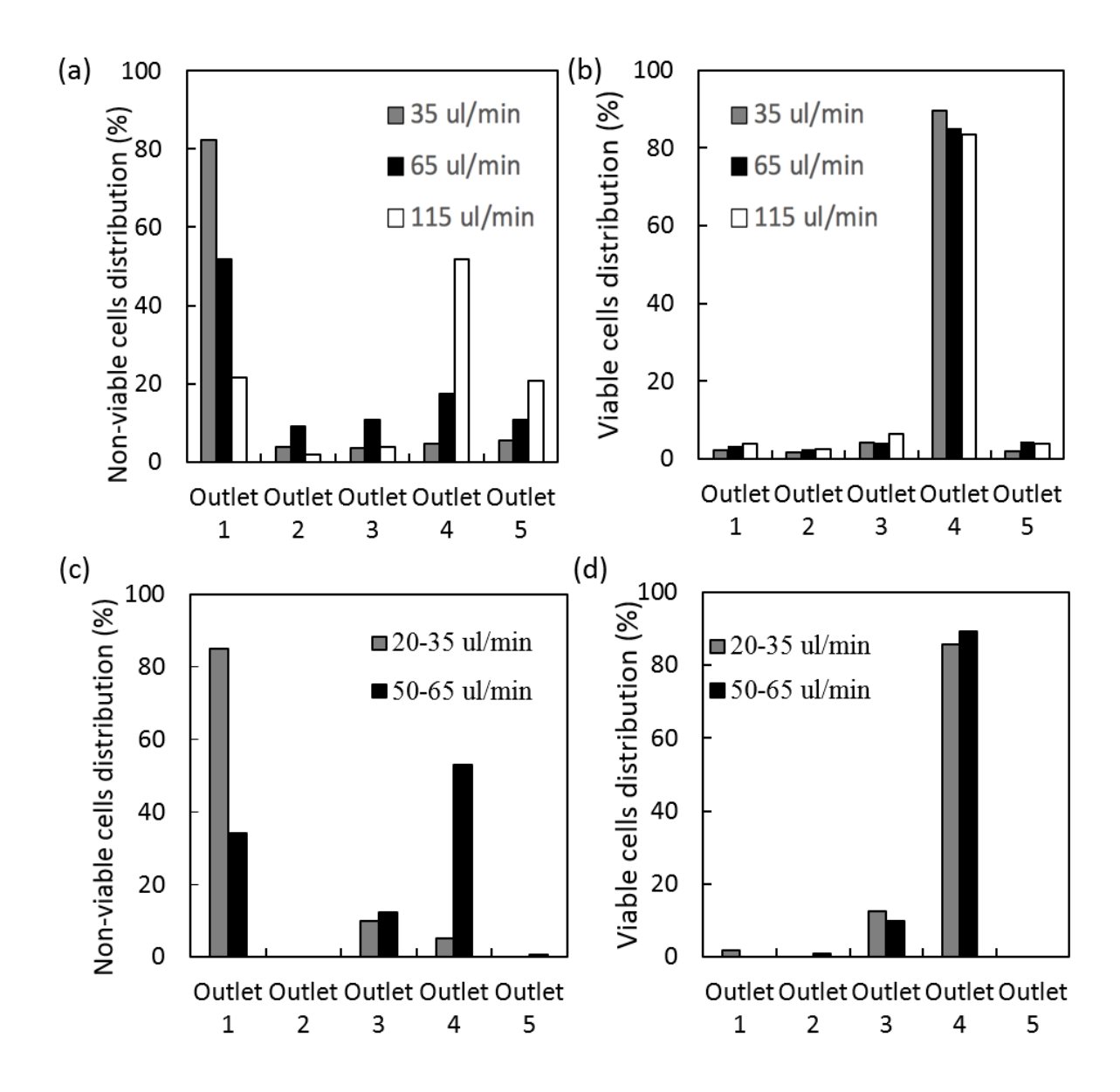


Figure 5: Non-viable (a) and Viable (b) Jurkat cells distribution at the five different outlets after sorting. Cells were flown at three different flow rates: 35 μ l/min, 65 μ l/min, and 115 μ l/min in a device with 20° ridge angle. Non-viable (c) and Viable (d) SUDHL cells distribution at the five different outlets after sorting, at two different flow rate ranges: 20-35 μ l/min and 50-65 μ l/min.

The displacement of viable cells is not sensitive to these ranges of flow rate as shown in Fig. 5b and Fig. 5d. In fact, by increasing the flow rate, the hydrodynamic force on the cells increases, increasing the number of cells that migrate toward the soft outlets and resulting in a weaker separation. Note that it may be possible to increase the recovery of non-viable cells at higher flow rates by using smaller ridge angles (not evaluated in this study). On the other hand, using too low flow rates (e.g. less than 20 μ l/min) can lead to slow passage of cells through the ridge region. Thus, the most efficient separation of viable and non-viable cells occurs at a total flow rate of 35 μ l/min, which is used in the rest of the experiments, unless specified otherwise. The cell sample was infused at 5 μ l/min, whereas the flow buffer was infused at 20 and 10 μ l/min respectively into the left and the right sheath inlets (top and bottom in Fig. 1) to position the focused cells off-center in the channel.

Transient adhesion between cells and microchannel surfaces can affect cell trajectory (39). The magnitude of the adhesion can be modified by using surface treatments. In occasional events, we observed adhesion of non-viable cells to the microfluidic channel surface that caused an increased ridge interaction time and a pile up of the cells near the ridges. Such events can negatively affect the separation outcomes and can lead to channel occlusion. To minimize non-specific cell binding, we passivated the microchannel interior with chemical vapor deposition of Triethoxysilane (3-Aminopropyl) instead of the BSA passivation. Silanes are generally known to form self-assembled monolayers when deposited onto a glass surface (40) and thus offer a simple way to change the surface properties through display of specific functional groups (41). It was found that APTES preserves the viability and proliferation of human dermal fibroblast (42) and does not deteriorate the potency of mesenchymal stem cells (43). To validate this surface treatment, we flow non-viable cells through a device with a ridge angle of 15° with and without the Triethoxysilane treatment. We noticed that the minimum flow rate that can be sustained in the silanized device is half the flow rate of the non-silanized. To quantitatively compare both passivation conditions, we evaluated the cell interaction time with the ridges. In the non-silanized device, the median value of interaction time is found to be 25 ms, whereas for the silanized device, it decreases to 5 ms, as shown in Fig. 6. Lower interaction times indicate the cells flow more easily through the constrictions leading to lower variability and enhanced separation.

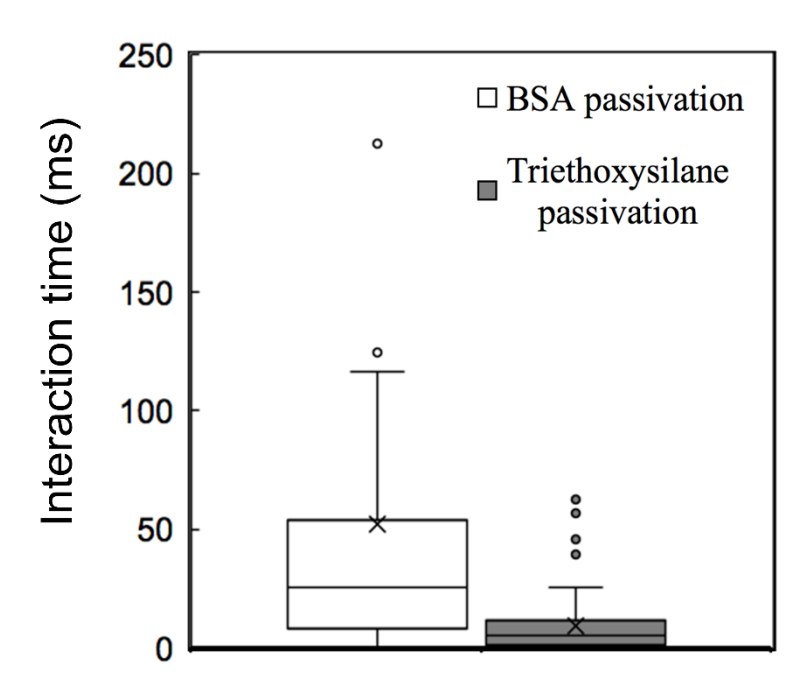


Figure 6: Interaction time of non-viable Jurkat cells with ridges in two 15° ridge angle devices, with and without Triethoxysilane passivation at the minimum flow rate that prevents channel clogging.

Cell separation and enrichment in the microfluidic device

A mixture of viable and non-viable cells at a 1: 1 ratio was flowed through the device and cells were collected from the five outlets and analyzed using flow cytometry. Based on the results of our optimization study, we use a flow rate of 35 μ l/min in a channel with 15° ridges. The separation is quantified in terms of the enrichment factor defined as the ratio of viable and non-viable cells at each outlet and at the inlet:

$$Enrichment\ Factor = \frac{\left(\frac{\%\ of\ Targeted\ cells}{\%\ of\ Non\ Targeted\ cells}\right)_{outlet}}{\left(\frac{\%\ of\ Targeted\ cells}{\%\ of\ Non\ Targeted\ cells}\right)_{inlet}}$$

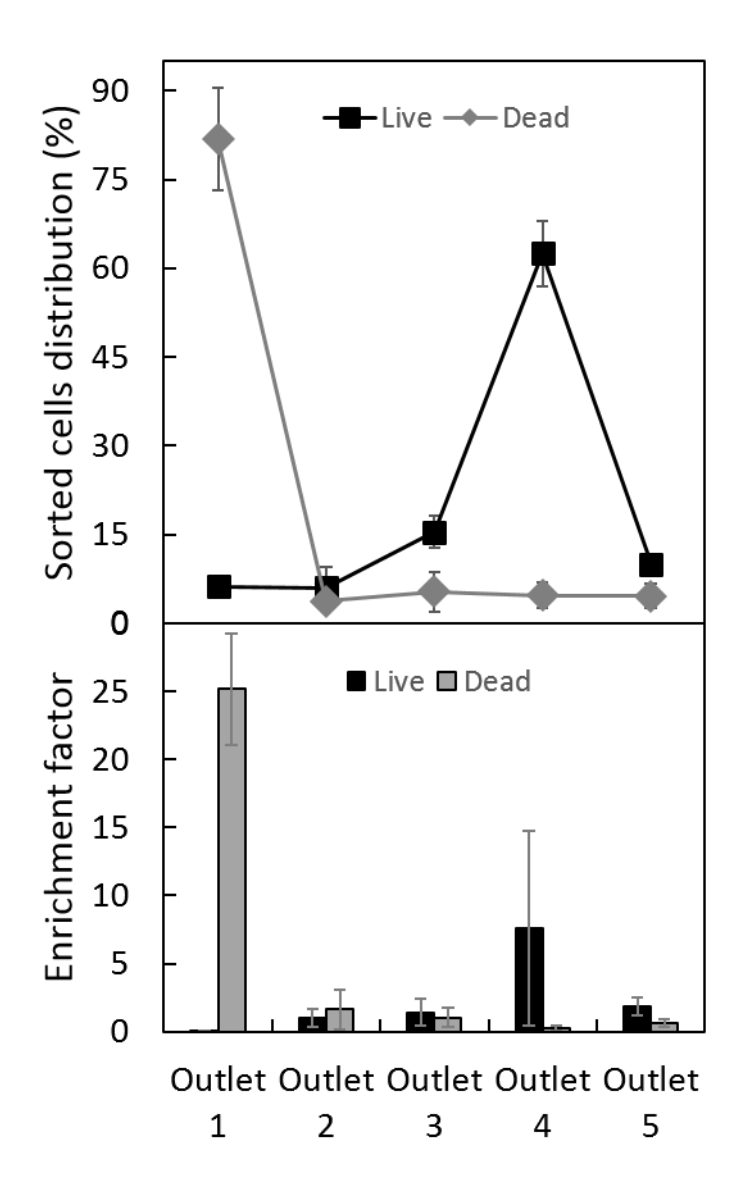


Figure 7: Sorted cells distribution (scatter line) and enrichment factor (histograms) of viable and nonviable cells populations, flowed at 35 μ l/min flow rate and in a device with a 15° ridge angle.

Sorting performance can also be assessed by cells recovery and purity defined as:
$$Recovery = \frac{(\# of \ Targeted \ cells)_{outlet}}{\sum_{all \ Outlets} (\# of \ Targeted \ cells)_{outlet}}$$

$$Purity = \frac{(\# of \ Targeted \ cells)_{outlet}}{(\sum \# of \ all \ cells)_{outlet}}$$

We quantified the sensitivity of the sorting to viability by examining the sorting distribution of viable and heat-treated cell populations. The metrics are plotted in Fig. 7 as an average from three repeated experiments and presented in Table 1. From the cell distribution, 81.78% of the non-viable cells translated towards the stiff outlet 1 and 62.48% of viable cells translated to the soft outlet 4 with a purity of 82.8%. Combining the cells from the two soft outlets 4 and 5 leads to a viable cell recovery of 72.4% with a purity of 78.7%. By including cells from the middle outlet 3, viable cell recovery can be increased to 87.8% with a purity of 74.1%. The average enrichment for viable and non-viable cells is 7.6 and 25.2 in outlets 4 and 1, respectively.

Table 1: Sorted cells distribution of viable and non-viable Jurkat cell populations at a flow rate of 35μ l/min and in a device with 15° ridge angle.

Sorted cells distribution (%)		
Ports	Non-viable	Viable
Outlet 1	81.78	6.20
Outlet 2	3.70	6.01
Outlet 3	5.26	15.37
Outlet 4	4.66	62.48
Outlet 5	4.60	9.94

Viability sensing mode through cell tracking

The microfluidic device can separate a mixed stream of viable and non-viable cells using the differences in their mechanical properties. An additional mode of sensing can use the information contained in trajectories of individual cells to differentiate cell populations while they flow through the channel. We used a tracking algorithm to follow cell motion in videos obtained using a high-speed camera. We extracted the cell deflection per ridge and the interaction time for each ridge in the channel for populations of viable cells and non-viable cells flown separately through the device. The cumulative deflection of each cell population is shown in Fig. 8a. The average cumulative deflection of viable cells is $-53.3 \, \mu m$ indicating a negative migration to the soft outlets, whereas the non-viable cells resulted in an average cumulative deflection of $105.1 \, \mu m$ and a translation in the positive direction towards the stiff outlets ($p < 10^{-11}$ where p is the probability value of the null hypothesis for a conducted student t-test, n=156).

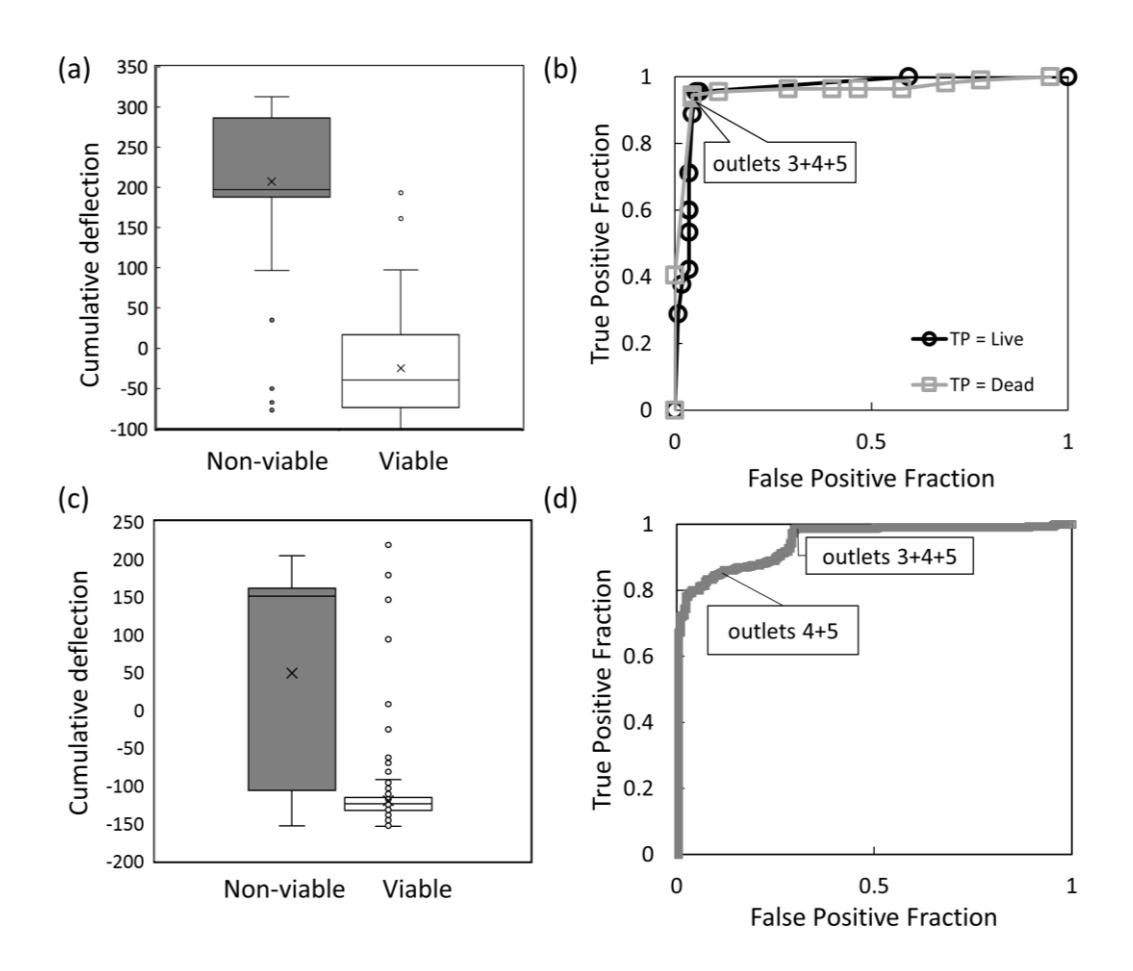


Figure 8: (a) Cumulative deflection of viable and non-viable Jurkat cells, calculated by summing the deflection of the cells at each ridge using the tracking algorithm. Cells were flowed at 35 µl/min in a device with 15° ridge angle. (b) Receiver Operator Characteristic (ROC) curves for the Jurkat cells deflection as a binary test classifier for two study cases. The black line is when viable cells are taken for positive, whereas the grey line is when non-viable cells are considered positive. (c) Contingency table used to separate test subjects into TPs, FPs, FNs, TNs based on cells deflection as a binary classifier. (d) ROC curve for SUDHL cells deflection as a binary test classifier for TP=Live.

We analyzed the cumulative deflection of cells to assess the utility of a single sensor output to differentiate viable and non-viable cells. The True-Positive Fraction (TPF) and False-Positive Fraction (FPF) were used to evaluate the binary classification of cells based on their deflection. Two case studies with different definitions of positive state were considered to illustrate the possible applications. The first case considered viable cells as positive and non-viable cells as negative (TP=viable), whereas the second case considered non-viable cells as positive and viable cells as negative (TP=non-viable). For the first case, a test outcome was considered positive if the cell deflection was below the threshold value, and for the second case, it was positive if the cell deflection was above the threshold value, for the full range of the deflection threshold values.

ROC curves were plotted by determining the true and false positive rates for the two study cases, as shown in Fig. 8b. The area under the Receiver Operator Characteristic (ROC) curve was used to calculate an area under the curve (AUC) to indicate the utility of the test, in which a perfect test has an AUC of 1. For the cumulative cell deflection used as a binary classifier, the AUC value was 0.97 for the first case (TP= viable) and 0.98 for the second case (TP=non-viable). Depending on the application, different outlets can be collected and combined to get the required sensitivity and specificity. For example, by collecting outlets 3, 4, and 5 in the first case (TP= viable), we can obtain a sensitivity of 96% and a specificity of 95%.

As another example of monitoring cell viability, SUDHL cells were heat-treated to induce cell death and a ROC curve produced from the separation data is shown in Fig. 8d. The AUC value was 0.95. Thus, the technology is able to sort and sense viable cells in a label-free and accurate manner comparable to commonly used cell viability stains and conventional apoptosis assays, for example propidium iodide (PI) which has been reported to significantly underestimate the viability of different types of cells (4-6).

Since the cumulative deflection reduces several cell-specific variables to a single parameter, there could be even more benefit in examining the trajectories of cells with more detail to determine the cell viability. We therefore used the cell size, deflection (Dx), and interaction time (Tx) at each ridge (x) as input variables to perform a dimensionality reduction using a principal component analysis (PCA) to further explore the clustering of viable and non-viable cells populations. We reduce the 11 variables to two dimensions as shown in Fig. 9. A clustering of the viable cell population with the PCA showed no overlap with the clustering from the non-viable cell population, suggesting that the detection could be even more accurate. The principal components PC1 and PC2 respectively explain 23% and 19.8% of the total variance. From the loading of each of the variables in the reduced data space, we notice that the interaction time with a ridge correlates with the deflection on the next ridge, for example T1 correlates with D2 and T2 correlates with D3. It is also observed that viable cells cluster to a single location while the non-viable cells cluster to three regions of the plot by the ridge where they deflect. It should be noted that all three clusters of the non-viable cells ended at the same outlet. However, PCA can be used to identify different routes of cell translation and possibly subsets of non-viable cells that are not distinguished by collecting from outlets.

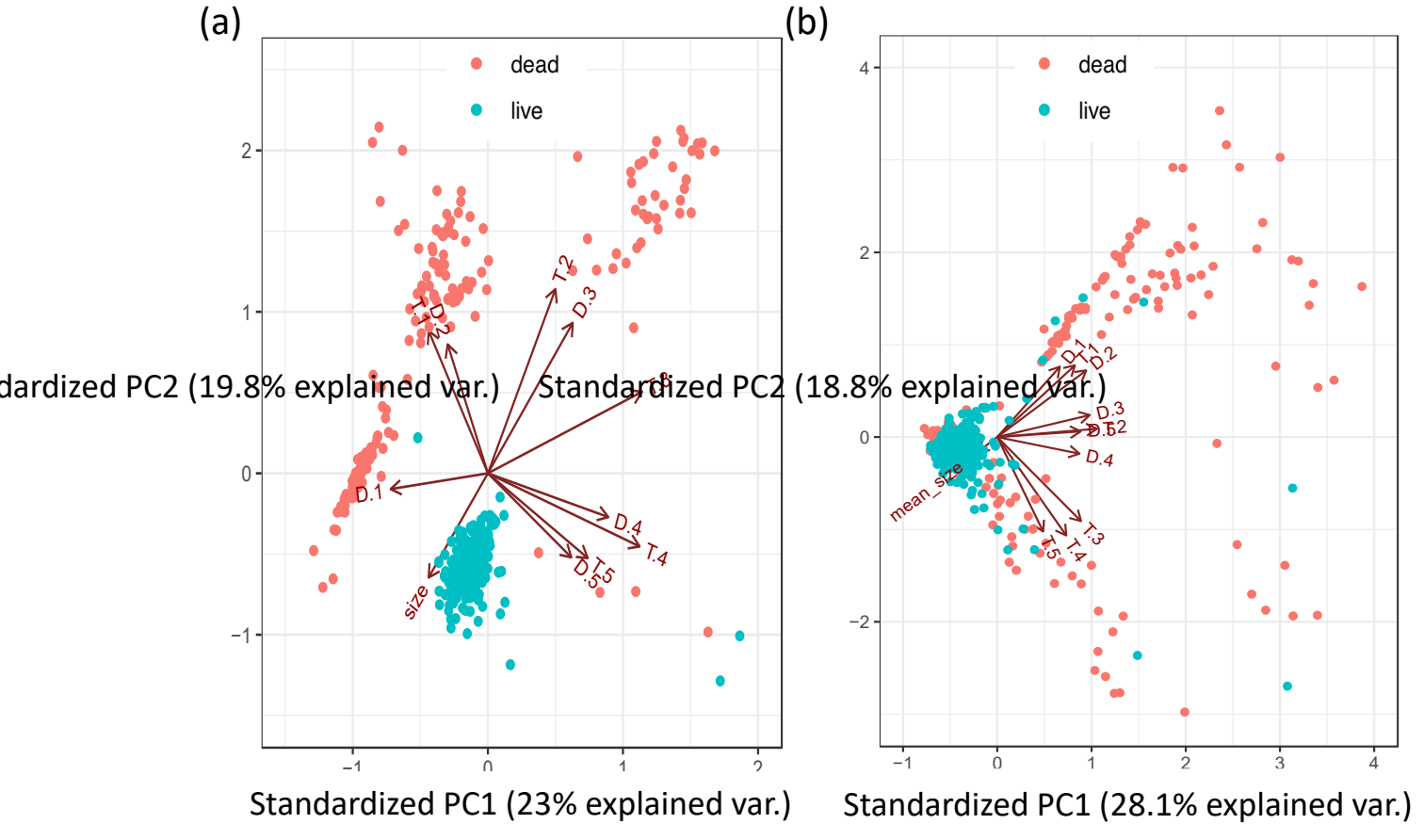


Figure 9: PCA analysis of non-viable and viable (a) Jurkat and (b) SUDHL cells using different features: cells deflection at each ridge, cells interaction time with each ridge and cells size. A total of 489 Jurkat cells and 650 SUDHL cells were analyzed.

As a comparison to other microfluidic-based systems, our work achieves high sorting accuracy for detection of cell viability (AUC of 0.97). In terms of comparison to the Guzniczak et al. study (44), they reported a recovery value of 60%, whereas our study can achieve up to 88% by combining outlets. Thus the multi-outlet device design we present in this study can lead to greater accuracy in separation. In terms of throughput, Islamzada et al. (45) reported a sorting throughput of 600 enucleated cells/min, whereas Guzniczak et al. (44) performed sorting at a capacity for high throughput of 3 10^6 cells/min at a concentration of 10^6 cells/mL. The separation and detection presented in this study is optimized for accuracy, not throughput. In this study, the throughput is 7.5 10^4 cells/min per channel at a concentration of $1 - 1.5 \cdot 10^6$ cells/mL. The sorting throughput can be increased by accepting a lower accuracy (e.g. AUC<0.97), or through channel multiplexing. In terms of device operation, our microfluidic platform can operate continuously over the course of several hours. However, the video readout and processing is currently limited to record several videos at different timepoints, thus limiting the number of data collection points.

Conclusion

We find that viable cells have distinct differences of biomechanical properties from non-viable cells that can be used for continuous cell separation and sensing. We demonstrate how a microfluidic cell separation device can be optimized for high sensitivity to biomechanical differences to detect viable and non-viable cells. We demonstrate two modes of sensing to transduce signals while cells are continuously flow through the device. We demonstrate that additional sensor outputs can be extracted and used to sense cell viability. We show in a sensitivity analysis that a single sensor output of "cumulative separation" produces an AUC of 0.97. Alternatively, a plethora of individual variables, including deflection per ridge, interaction time at each ridge, and cell size, can all be used in a PCA to provide a greater capacity to cluster cells with no overlap between viable and non-viable subpopulations. This approach can thus be used as a new type of label-free sensor for monitoring of cell viability and functional health of cell cultures.

Supporting Information

Supporting Information Available: The following files are available free of charge.

- S1 viable Jurkat 15deg.mp4: Video of viable Jurkat cells in a 15° ridge angle device.
- S2_nonViable_Jurkat_15deg.mp4: Video of non-viable Jurkat cells in a 15° ridge angle device.
- S3_nonViable_Jurkat_30deg .mp4: Video of non-viable Jurkat cells in a 30° ridge angle device showing the cell gradual displacement mode.

Acknowledgments

Support from NSF Engineering Research Center for Cell Manufacturing Technologies and the NSF Award CBET-1928262 is gratefully acknowledged.

References:

- 1. Nagy A, Rossant J, Nagy R, Abramow-Newerly W, Roder JC. Derivation of completely cell culture-derived mice from early-passage embryonic stem cells. Proceedings of the National Academy of Sciences. 1993;90(18):8424-8.
- 2. Joza N, Susin SA, Daugas E, Stanford WL, Cho SK, Li CY, Sasaki T, Elia AJ, Cheng H-YM, Ravagnan L. Essential role of the mitochondrial apoptosis-inducing factor in programmed cell death. Nature. 2001;410(6828):549-54.
- 3. Islam M, Mezencev R, McFarland B, Brink H, Campbell B, Tasadduq B, Waller EK, Lam WA, Alexeev A, Sulchek T. Microfluidic cell sorting by stiffness to examine heterogenic responses of cancer cells to chemotherapy. Cell Death and Disease. 2018:accepted.
- 4. Rosenberg M, Azevedo NF, Ivask A. Propidium iodide staining underestimates viability of adherent bacterial cells. Scientific reports. 2019;9(1):1-12.
- 5. Kirchhoff C, Cypionka H. Propidium ion enters viable cells with high membrane potential during live-dead staining. Journal of microbiological methods. 2017;142:79-82.
- 6. Rieger AM, Hall BE, Schang LM, Barreda DR. Conventional apoptosis assays using propidium iodide generate a significant number of false positives that prevent accurate assessment of cell death. Journal of immunological methods. 2010;358(1-2):81-92.
- 7. Hunsberger J, Harrysson O, Shirwaiker R, Starly B, Wysk R, Cohen P, Allickson J, Yoo J, Atala A. Manufacturing road map for tissue engineering and regenerative medicine technologies. Stem Cells Translational Medicine. 2015;4(2):130-5.
- 8. Consortium NCM. Achieving Large-Scale, Cost-Effective, Reproducible Manufacturing of High Quality Cells. A Technology Roadmap to. 2016;2025:92-101.
- 9. Chen W, Frank ME, Jin W, Wahl SM. TGF-β released by apoptotic T cells contributes to an immunosuppressive milieu. Immunity. 2001;14(6):715-25.
- 10. Hessler JA, Budor A, Putchakayala K, Mecke A, Rieger D, Banaszak Holl MM, Orr BG, Bielinska A, Beals J, Baker J. Atomic force microscopy study of early morphological changes during apoptosis. Langmuir. 2005;21(20):9280-6.
- 11. Meng F-y, Chen Z-s, Han M, Hu X-p, Zhou P. An improved purification approach with high cell viability and low cell loss for cryopreserved hepatocytes. Cryobiology. 2010;60(2):238-9.
- 12. Cerf A, Cau J-C, Vieu C, Dague E. Nanomechanical properties of dead or alive single-patterned bacteria. Langmuir. 2009;25(10):5731-6.
- 13. Rafaï S, Jibuti L, Peyla P. Effective viscosity of microswimmer suspensions. Phys Rev Lett. 2010;104(9):098102.
- 14. Frame KK, Hu WS. Cell volume measurement as an estimation of mammalian cell biomass. Biotechnol Bioeng. 1990;36(2):191-7.
- 15. Patel S, Showers D, Vedantam P, Tzeng T-R, Qian S, Xuan X. Microfluidic separation of live and dead yeast cells using reservoir-based dielectrophoresis. Biomicrofluidics. 2012;6(3):034102.
- 16. Shafiee H, Sano MB, Henslee EA, Caldwell JL, Davalos RV. Selective isolation of live/dead cells using contactless dielectrophoresis (cDEP). Lab Chip. 2010;10(4):438-45.
- 17. Jen C-P, Chen T-W. Selective trapping of live and dead mammalian cells using insulator-based dielectrophoresis within open-top microstructures. Biomedical microdevices. 2009;11(3):597.

- 18. Filice FP, Henderson JD, Li MS, Ding Z. Correlating Live Cell Viability with Membrane Permeability Disruption Induced by Trivalent Chromium. ACS omega. 2019;4(1):2142-51.
- 19. Alam JM, Kobayashi T, Yamazaki M. The single-giant unilamellar vesicle method reveals lysenin-induced pore formation in lipid membranes containing sphingomyelin. Biochemistry-Us. 2012;51(25):5160-72.
- 20. Schmidt MC, Rothen-Rutishauser B, Rist B, Beck-Sickinger A, Wunderli-Allenspach H, Rubas W, Sadée W, Merkle HP. Translocation of human calcitonin in respiratory nasal epithelium is associated with self-assembly in lipid membrane. Biochemistry-Us. 1998;37(47):16582-90.
- 21. Doh I, Cho Y-H. A continuous cell separation chip using hydrodynamic dielectrophoresis (DEP) process. Sensors and Actuators A: Physical. 2005;121(1):59-65.
- 22. Yang AH, Soh HT. Acoustophoretic sorting of viable mammalian cells in a microfluidic device. Anal Chem. 2012;84(24):10756-62.
- 23. Zhang S, Wang Y, Onck P, den Toonder J. A concise review of microfluidic particle manipulation methods. Microfluid Nanofluid. 2020;24(4):1-20.
- 24. Lam WA, Rosenbluth MJ, Fletcher DA. Chemotherapy exposure increases leukemia cell stiffness. Blood. 2007;109(8):3505-8.
- 25. MacQueen LA, Thibault M, Buschmann MD, Wertheimer MR. Electromechanical deformation of mammalian cells in suspension depends on their cortical actin thicknesses. J Biomech. 2012;45(16):2797-803.
- 26. Islam M, Brink H, Blanche S, DiPrete C, Bongiorno T, Stone N, Liu A, Philip A, Wang G, Lam W, Alexeev A, Waller EK, Sulchek T. Microfluidic Sorting of Cells by Viability Based on Differences in Cell Stiffness. Scientific reports. 2017;7(1):1997.
- 27. Nikolaev NI, Müller T, Williams DJ, Liu Y. Changes in the stiffness of human mesenchymal stem cells with the progress of cell death as measured by atomic force microscopy. J Biomech. 2014;47(3):625-30.
- 28. Zhou Y, Yang D, Zhou Y, Khoo BL, Han J, Ai Y. Characterizing deformability and electrical impedance of cancer cells in a microfluidic device. Anal Chem. 2018;90(1):912-9.
- 29. Otto O, Rosendahl P, Mietke A, Golfier S, Herold C, Klaue D, Girardo S, Pagliara S, Ekpenyong A, Jacobi A. Real-time deformability cytometry: on-the-fly cell mechanical phenotyping. Nature methods. 2015;12(3):199-202.
- 30. Deng Y, Davis SP, Yang F, Paulsen KS, Kumar M, Sinnott DeVaux R, Wang X, Conklin DS, Oberai A, Herschkowitz JI. Inertial microfluidic cell stretcher (iMCS): fully automated, high-throughput, and near real-time cell mechanotyping. Small. 2017;13(28):1700705.
- 31. Wang GH, Crawford K, Turbyfield C, Lam W, Alexeev A, Sulchek T. Microfluidic cellular enrichment and separation through differences in viscoelastic deformation. Lab Chip. 2015;15(2):532-40. doi: Doi 10.1039/C4lc01150c. PubMed PMID: WOS:000346477500018.
- 32. Xu W, Chahine N, Sulchek T. Extreme hardening of PDMS thin films due to high compressive strain and confined thickness. Langmuir. 2011;27(13):8470-7. doi: 10.1021/la201122e.
- 33. Haase K, Pelling AE. Investigating cell mechanics with atomic force microscopy. J R Soc Interface. 2015;12(104):20140970.
- 34. Moreno-Flores S, Benitez R, dM Vivanco M, Toca-Herrera JL. Stress relaxation and creep on living cells with the atomic force microscope: a means to calculate elastic moduli and viscosities of cell components. Nanotechnology. 2010;21(44):445101.
- 35. Bongiorno T, Chojnowski JL, Lauderdale JD, Sulchek T. Cellular stiffness as a novel stemness marker in the corneal limbus. Biophysical journal. 2016;111(8):1761-72.

- 36. Jeong J, Frohberg NJ, Zhou E, Sulchek T, Qiu P. Accurately tracking single-cell movement trajectories in microfluidic cell sorting devices. PloS one. 2018;13(2):e0192463.
- 37. Kim KS, Cho CH, Park EK, Jung M-H, Yoon K-S, Park H-K. AFM-detected apoptotic changes in morphology and biophysical property caused by paclitaxel in Ishikawa and HeLa cells. PloS one. 2012;7(1):e30066.
- 38. Wang GH, Mao WB, Byler R, Patel K, Henegar C, Alexeev A, Sulchek T. Stiffness Dependent Separation of Cells in a Microfluidic Device. Plos One. 2013;8(10):e75901. doi: ARTN e75901
- DOI 10.1371/journal.pone.0075901. PubMed PMID: WOS:000326019400022.
- 39. Tasadduq B, Mcfarland B, Islam M, Alexeev A, Sarioglu AF, Sulchek TA. Continuous sorting of cells based on differential P selectin glycoprotein ligand expression using molecular adhesion. Anal Chem. 2017.
- 40. Ting LH, Feghhi S, Han SJ, Rodriguez ML, Sniadecki NJ. Effect of silanization film thickness in soft lithography of nanoscale features. Journal of Nanotechnology in Engineering and Medicine. 2011;2(4).
- 41. Hen M, Ronen M, Deitch A, Barbiro-Michaely E, Oren Z, Sukenik CN, Gerber D. An off-the-shelf integrated microfluidic device comprising self-assembled monolayers for protein array experiments. Biomicrofluidics. 2015;9(5):054108.
- 42. Aithal RK, Doss AT, Kumaraswamy DP, Mills DK, Kuila D. Growth and Functionality of Cells Cultured on Conducting and Semi-Conducting Surfaces Modified with Self-Assembled Monolayers (SAMs). Coatings. 2016;6(1):9.
- 43. Chuah YJ, Kuddannaya S, Lee MHA, Zhang Y, Kang Y. The effects of poly (dimethylsiloxane) surface silanization on the mesenchymal stem cell fate. Biomaterials science. 2015;3(2):383-90.
- 44. Guzniczak E, Otto O, Whyte G, Willoughby N, Jimenez M, Bridle H. Deformability-induced lift force in spiral microchannels for cell separation. Lab Chip. 2020;20(3):614-25.
- 45. Islamzada E, Matthews K, Guo Q, Santoso AT, Duffy SP, Scott MD, Ma H. Deformability based sorting of stored red blood cells reveals donor-dependent aging curves. Lab Chip. 2020;20(2):226-35.

For TOC only

